(Received 11 May 2026, Accepted 10 June 2026, Scheduled 24 June 2026)

Mode-Orthogonal Dual-Band Antenna Pair with High Isolation

Bowen Song[1], Han Lin[1,*], Zhonggen Wang[1], and Wenyan Nie[2]

[1] School of Electrical and Information Engineering, Anhui University of Science and Technology, Huainan 232001, China
[2] School of Mechanical and Electrical Engineering, Huainan Normal University, Huainan 232001, China

ABSTRACT: To meet the multi-band coverage requirements of 5G smartphones, this paper presents a dual-band antenna pair with high isolation. Based on the principle of mode orthogonality, a T-shaped dual-arm antenna and a bent-loop antenna are integrated within the smartphone frame, enabling excitation of multiple in-phase and anti-phase modes across the two target frequency bands. Under a closely spaced arrangement and without requiring additional decoupling structures, the antenna pair achieves superior isolation exceeding 20 dB. A multiple-input multiple-output (MIMO) antenna array, formed by symmetrically arranging four such antenna pairs, covers the 3.4–3.6 GHz and 5.1–5.76 GHz bands. The isolation across both bands remains better than 15 dB, with efficiencies exceeding 70% and 72%, respectively. The array supports 5G n77/n78 and Wi-Fi frequency bands, and the envelope correlation coefficient (ECC) between ports is below 0.04, demonstrating favorable spatial diversity performance. The proposed MIMO antenna array features a compact form factor and excellent isolation, enabling multi-antenna integration, dual-band operation, and self-decoupling within a limited volume. This design provides a technical reference for future multi-band, multi-antenna system development in 5G mobile terminals.

1. INTRODUCTION

With the rapid advancement of fifth-generation (5G) mobile communication technology, wireless communication systems are required to achieve higher data rates and enhanced transmission reliability, thereby imposing increasingly stringent demands on antenna performance. MIMO technology, as one of the most widely adopted key enablers in 5G, significantly improves spectral efficiency and channel capacity, laying the foundation for high-throughput communications [1–3]. However, while MIMO antenna systems deliver superior communication capabilities, they also substantially increase the number of antenna elements, which intensify mutual coupling among closely spaced radiators and consequently degrade overall antenna performance. Therefore, the design of MIMO antennas that integrate multi-band operation and self-decoupling capability within a limited volume has emerged as a central challenge in contemporary antenna engineering.

To mitigate coupling effects among MIMO antenna elements, various decoupling methods have been proposed, which can be broadly classified into two categories. The first category involves the introduction of external decoupling structures, such as parasitic decoupling elements [4–6] and neutralization lines [7, 8]. However, conventional approaches of this kind typically suffer from low spatial reuse efficiency and often require additional occupied area, hindering the realization of highly integrated devices. The second category encompasses self-decoupling techniques, including polarization orthogonality [9], mode cancellation principles [10–12], and mode orthogonality principles [13, 14], which are capable of achieving high isolation between densely arranged antennas. Nevertheless, most of these methods have been confined to single narrowband operation. Recently, research efforts have been progressively extended toward wideband [15] and dual-band antenna implementations [16, 17]. For instance, in [18], a coplanar waveguide (CPW)-fed structure composed of a T-shaped monopole and a T-shaped slot was employed to excite odd and even modes, thereby generating orthogonal characteristic modes and achieving high isolation without the need for clearance. In [19], a differential-mode antenna was integrated with a loop branch, and the parasitic branch naturally introduced a second transmission zero, enabling simultaneous mode-orthogonal decoupling and parasitic decoupling for wideband high isolation without requiring a differential feeding network. In [20], based on the mode orthogonality principle, dual-band self-decoupling was realized through the orthogonality of multiple sets of in-phase and anti-phase current modes. In [21], four hybrid modes are employed, and dual-band self-decoupling is achieved through the mode cancellation principle under odd and even mode excitations, while wideband self-decoupling is simultaneously obtained by narrowing the frequency spacing between the two bands. Despite the progress demonstrated by these methods, limitations such as insufficient isolation and relatively weak spatial diversity performance persist. Therefore, for highly integrated antenna pairs, realizing dual-band high isolation within the extremely compact frame of a smartphone without introducing additional structures remains a significant design challenge.

To address the aforementioned challenges, this paper presents a high-isolation dual-band antenna pair designed for 5G smartphone applications. Based on the principle of mode orthogonality, a T-shaped dual-arm antenna and a bent-loop antenna are integrated within the tightly arranged smartphone space, enabling the excitation of multiple in-phase and anti-phase modes across two frequency bands and achieving isolation exceeding 20 dB. A MIMO antenna array, formed

* Corresponding author: Han Lin (hanlin@aust.edu.cn).

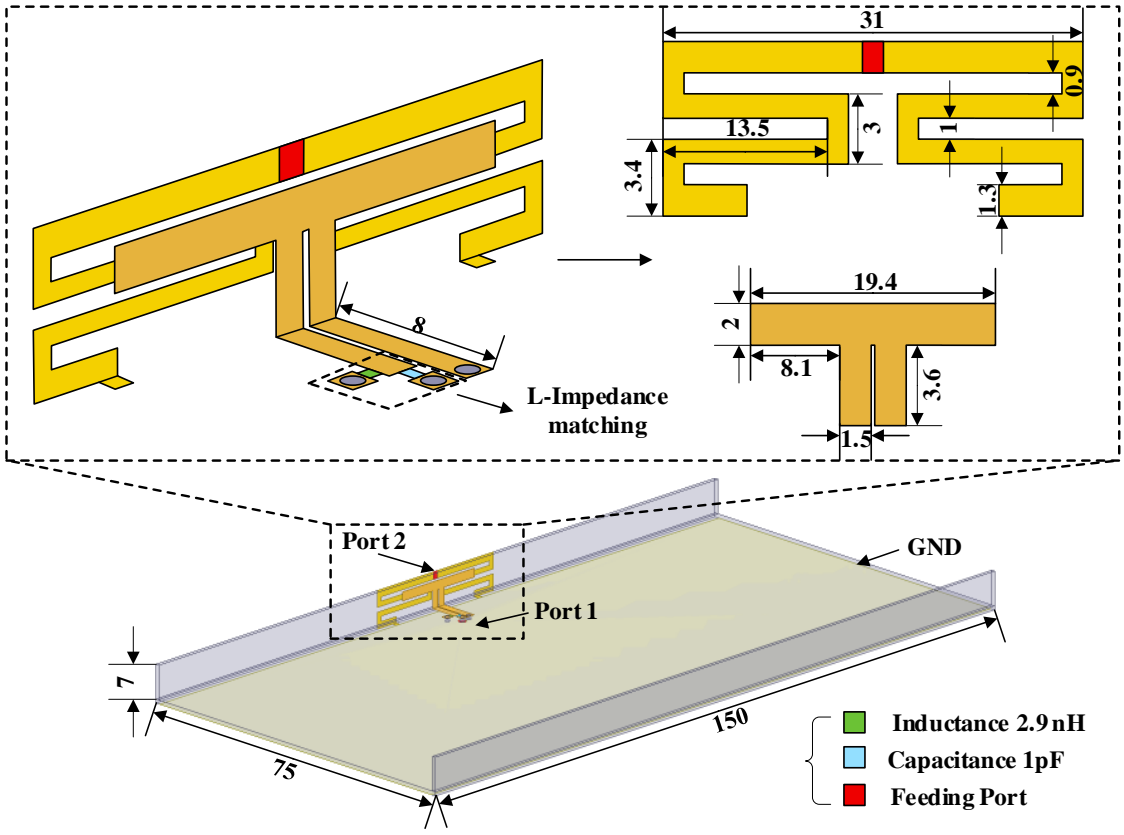

FIGURE 1. Geometry of the proposed mode-orthogonal antenna pair.

by symmetrically arranging four antenna pairs, delivers an isolation better than 15 dB and covers the 3.4–3.6 GHz and 5.1–5.76 GHz frequency bands. Furthermore, the system achieves total efficiencies exceeding 70% and 72% in the respective bands, with all envelope correlation coefficients (ECCs) between different ports remaining below 0.04, demonstrating favorable spatial diversity performance.

2. ANTENNA DESIGN

2.1. Antenna Configuration

Figure 1 illustrates the geometrical configuration of the proposed antenna pair. The design utilizes an FR4 dielectric substrate ($\varepsilon_r = 4.4$, $\tan\delta$ =0.02) with dimensions of $150 \times 75 \times 0.8\,\text{mm}^3$ as the main board, the back side of which is covered by a metallic ground plane measuring $150 \times 73\,\text{mm}^2$. Two FR4 side frames, each with dimensions of $150 \times 7 \times 0.8\,\text{mm}^3$, are mounted vertically along the edges of the main board. The antenna pair consists of a bent-loop antenna etched on the outer layer of the frame and a T-shaped dual-arm antenna etched on the inner layer. Specifically, the bent-loop antenna is excited via Port 2, whereas the T-shaped dual-arm element is fed through Port 1. To enhance impedance matching, an L-shaped matching network is incorporated into the microstrip feed line connected to Port 1. This matching network comprises a shunt inductor (2.9 nH) and a series capacitor (1 pF).

2.2. Evolution Process

To elucidate the design rationale of the dual-band antenna pair, Figure 2 illustrates its evolutionary process. As shown in Figures 2(a) and (b), the T-shaped dual-arm antenna etched on the inner layer of the side-edge frame operates over the frequency range of 3–4.16 GHz, whereas the loop antenna on the outer layer covers the bands of 3-3.06 GHz and 3.4–3.63 GHz. As depicted in Figure 2(c), integrating the T-shaped dual-arm antenna and bent-loop antenna within a compact volume shifts the operating bands to 3.5–3.6 GHz and 5.1–5.8 GHz. It can be observed that when Port 1 is excited, the T-shaped dual-arm antenna functions as a feeding branch of the bent-loop antenna, yielding a new resonant frequency at 5.2 GHz. When Port 2 is excited, the T-shaped dual-arm antenna acts as a parasitic branch of the bent-loop antenna, and due to the coupling effect, the bent-loop antenna produces an additional resonance at 5.6 GHz. However, at 3.5 GHz, the impedance matching performance of the T-shaped dual-arm antenna fails to meet the design specifications, rendering this band unusable. Consequently, an L-shaped impedance matching network is introduced at the feed port of the T-shaped dual-arm antenna to tailor its impedance matching characteristics, thereby forming the final proposed antenna pair. As shown in Figure 2(d), benefiting from the combined effect of the integrated design and the impedance matching network, the operating bands of the antenna pair are extended to 3.36–3.63 GHz and 5.1–5.76 GHz, with a port-to-port isolation exceeding 20 dB.

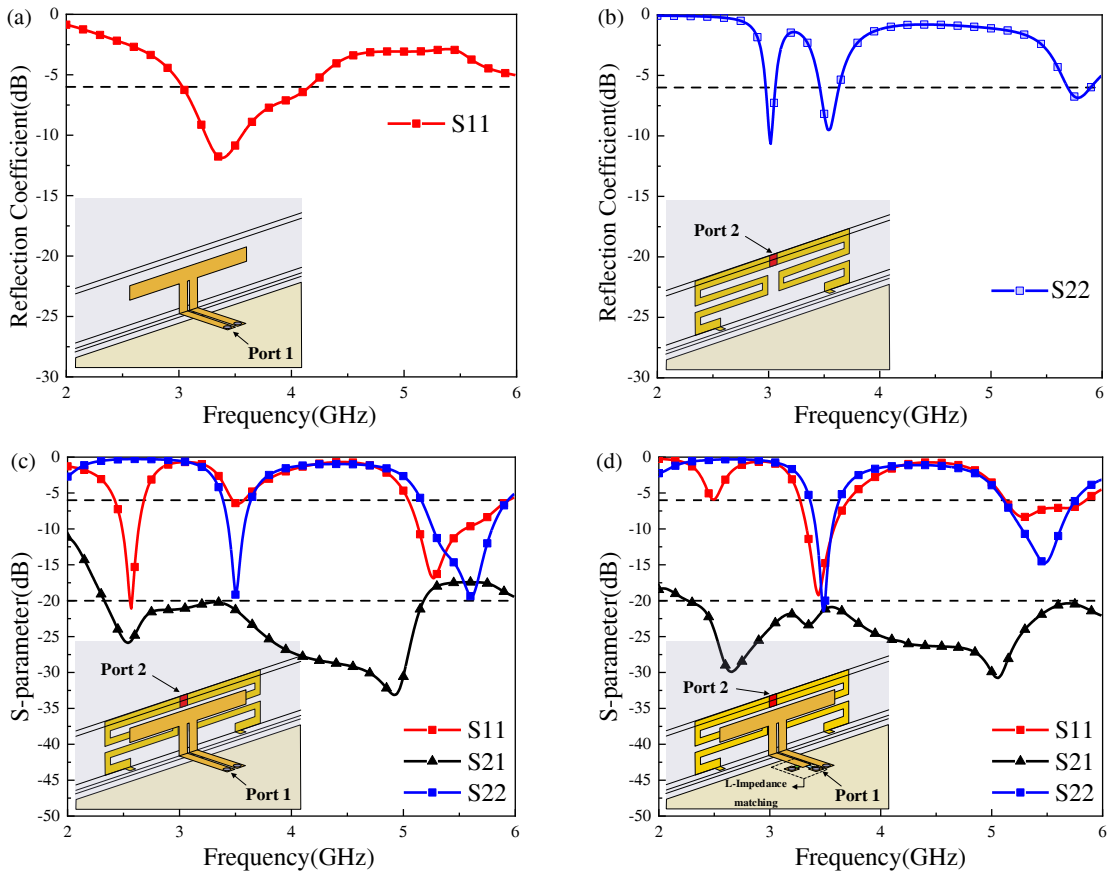

FIGURE 2. S-parameters of the evolution process. (a) T-shaped dual-arm antenna, (b) loop antenna, (c) antenna pair, and (d) L-type impedance matching network antenna pair.

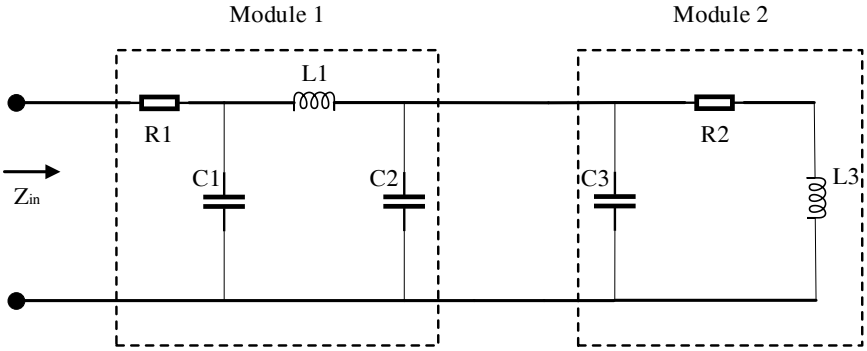

FIGURE 3. Equivalent circuit after loading the L-shaped impedance matching network.

Further analysis reveals that the inclusion of the L-shaped matching network shifts the original resonant frequency of the T-shaped dual-arm antenna from 2.6 GHz to 3.5 GHz, while the resonant frequency of the bent-loop antenna remains virtually unchanged. Despite the extremely close spacing between the two elements, high isolation is successfully achieved across both target frequency bands.

Figure 3 shows the equivalent circuit after loading the L-shaped impedance matching network. Figure 4 compares the Smith charts of the antenna before and after matching. In the figure, Module 1 represents the T-shaped dual-arm antenna without the matching network, where R_1 denotes the radiation resistance; C_1 and L_1 represent the inherent capacitive and inductive reactance, respectively; and the distributed capacitance C_2 is used to adjust the capacitive component. As shown in Figure 4(a), R_1, C_1, L_1, and C_2 jointly produce a lower frequency resonance. However, at 3.5 GHz, the overall input impedance of the antenna is capacitive, necessitating the introduction of inductive reactance through a matching network for compensation.

Module 2 corresponds to a T-shaped dual-arm antenna loaded with an L-shaped matching network, which consists of a shunt

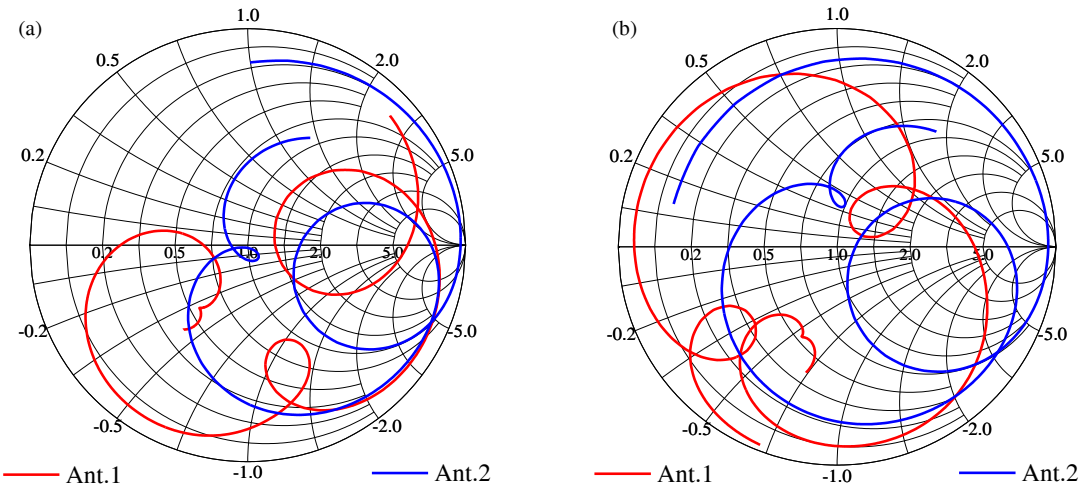

FIGURE 4. Smith charts of the antenna pair before and after matching. (a) before matching and (b) after matching.

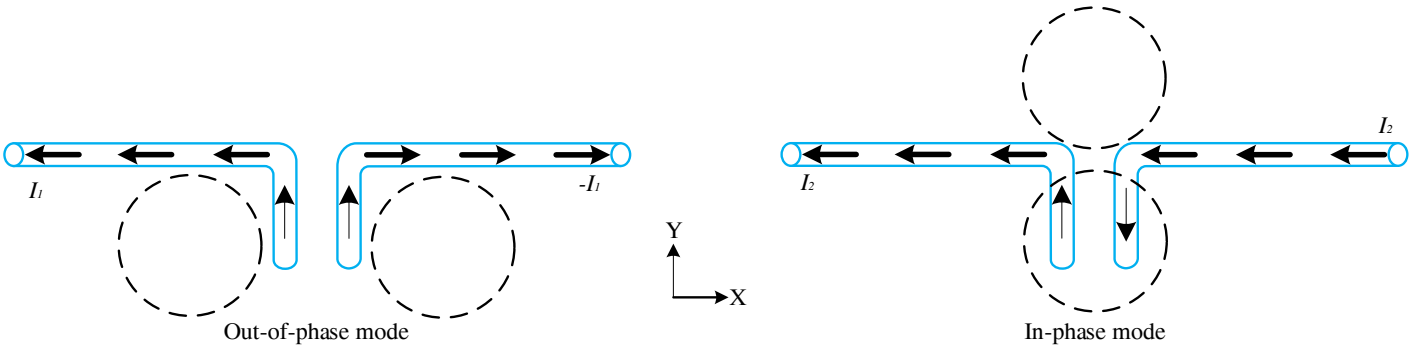

FIGURE 5. Current distribution characteristics under common-mode and differential-mode excitation.

capacitor C_3 and a series combination of a resistor R_2 and an inductor L_3. The series inductor L_3 increases the inductive component of the impedance, while the resistor R_2 allows the real part of the impedance to be tuned. Together with the shunt capacitor C_3, they cancel the capacitive behavior of the original antenna. As illustrated in Figure 4(b), through the tuning provided by the L-shaped matching network, the input impedance moves along a circle on the Smith chart, ultimately placing the impedance at the 3.5 GHz frequency point within the inductive region.

Meanwhile, the bent-loop antenna acts as a parasitic branch of the T-shaped dual-arm antenna. After matching, its high-frequency resonance shifts toward the inductive region, which shortens the usable high-frequency bandwidth. However, this frequency band precisely aligns with that of the T-shaped dual-arm antenna, so the effect of overmatching can be considered negligible.

2.3. Decoupling Mechanism

To elucidate the self-decoupling mechanism of the proposed antenna pair, an ideal mode orthogonality model is first established. As shown in Figure 5, a pair of ideal dipole antennas is taken as the reference. The decoupling mechanism originates from the inherent orthogonality between the radiation modes of the common-mode (CM) antenna and the differential-mode (DM) antenna. Under CM excitation, anti-phase currents of equal amplitude and opposite direction are induced on the CM antenna surface, which can be mathematically regarded as a symmetric function, denoted as I_1. The corresponding transverse radiation pattern features main lobes directed along the $\pm X$-axes. In contrast, under DM excitation, in-phase currents of equal amplitude and identical direction are generated on the DM antenna surface, which can be treated as a continuous function, denoted as I_2. Its transverse radiation pattern yields main lobes oriented along the $\pm Y$-axes.

When the two antenna types are integrated, the coupling contributions from the left and right halves are denoted as D_1 and D_2, respectively, and can be approximately expressed as:

$$D_1 = J \int_V f(I_1) \cdot f(I_2) dv \tag{1}$$

$$D_2 = J \int_V f(-I_1) \cdot f(I_2) dv \tag{2}$$

where J represents the current-related transformation coefficient, f the transformation function between the current and the corresponding radiated field, and v the effective volume of

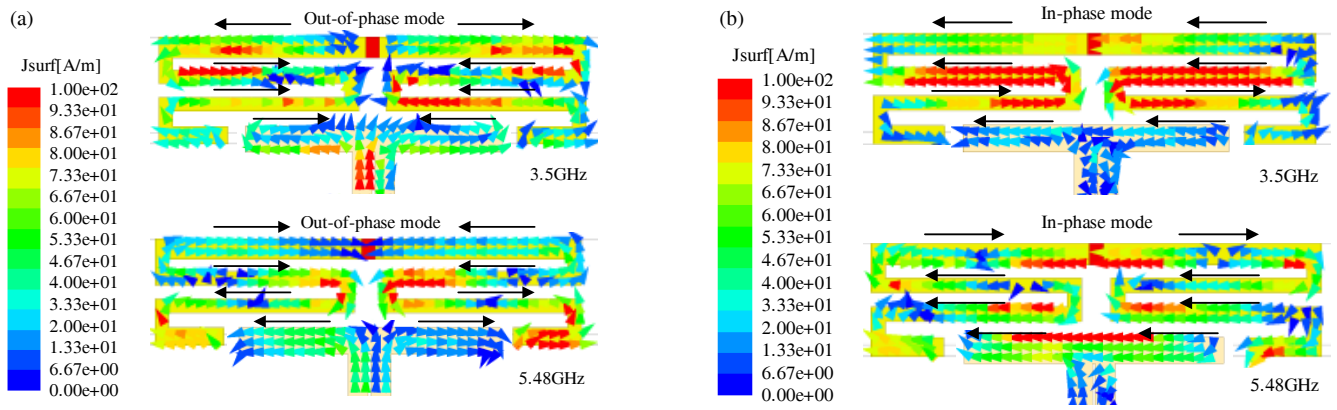

FIGURE 6. Simulation results of surface current distribution under different resonant modes. (a) Port 1 excitation and (b) port 2 excitation.

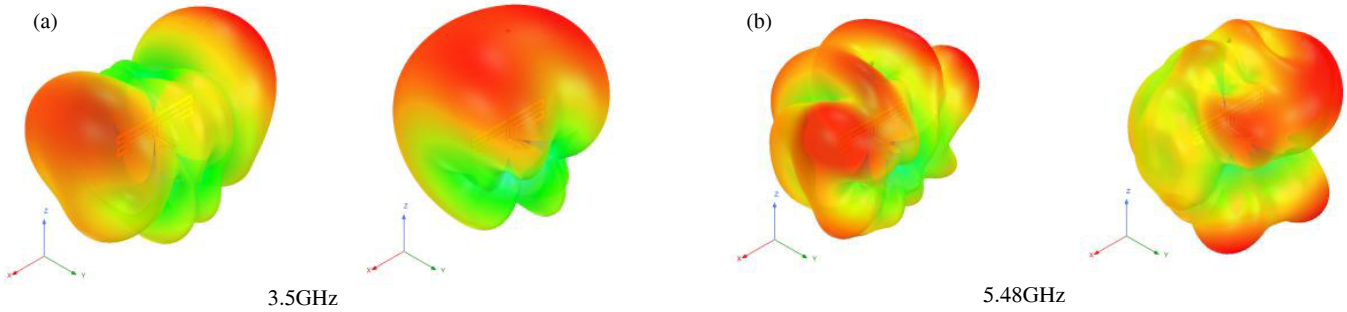

FIGURE 7. Simulation results of radiation patterns at different resonant frequencies. (a) 3.5 GHz and (b) 5.48 GHz.

the port region. Consequently, the total coupling strength D_T can be formulated as:

$$D_T = D_1 + D_2 \tag{3}$$

Under this configuration, the total coupling strength D_T between the two antenna elements can be approximately expressed as a superposition of two contributions. Owing to the symmetry of the CM current and the continuity of the DM current, their coupling effects in the near-field region cancel each other when integrated over the far field, thereby causing D_T to approach zero. This duality in the current distributions leads to pattern orthogonality: the direction of maximum radiation for the CM mode coincides with the radiation null of the DM mode, and vice versa. Consequently, the antenna pair achieves decoupling at the specific frequency f.

Figure 6 presents the simulated surface current distributions of the antenna pair when Port 1 and Port 2 are individually excited at 3.5 GHz and 5.48 GHz. We extend the principle revealed by the idealized model to a more sophisticated antenna design. As shown in Figure 6(a), when Port 1 is excited, the T-shaped dual-arm element acts as the primary radiator. Under the influence of the L-shaped impedance matching network, CM currents are generated on the T-shaped arms at 3.5 GHz, while the bent-loop antenna simultaneously exhibits a wavelength loop mode characterized by in-phase current distribution. Through far-field superposition, a radiation null is formed in the YOZ plane, and the energy is predominantly concentrated in the XOZ plane. When Port 2 is excited, as depicted in Figure 6(b), the bent-loop antenna serves as the primary radiator, exhibiting a DM current distribution with a quarter-wavelength ($\lambda/4$) resonant characteristic at 3.5 GHz, whereas the T-shaped dual-arm structure functions as a parasitic branch, coupling DM currents of opposite direction. The resulting far-field superposition produces a radiation null in the XOY plane, with the energy mainly concentrated in the XOZ plane. At 5.48 GHz, the modal current distribution patterns excited by each port are consistent with those observed at 3.5 GHz. This current distribution behavior is in good agreement with the modal current characteristic described in the theoretical analysis.

Figure 7 illustrates the simulated radiation patterns of the antenna pair when Port 1 and Port 2 are individually excited at 3.5 GHz and 5.48 GHz. When Port 1 is excited, the presence of CM currents causes the main lobe of the radiation pattern to be directed along the $\pm X$-axes. In contrast, when Port 2 is excited, the DM currents result in a radiation pattern with its main lobe oriented along the $\pm Y$-axes. While the antenna ports themselves may be arranged orthogonally, it is the orthogonality of the radiation patterns associated with different modes, not the port arrangement, that fundamentally gives rise to the high isolation. This consistency confirms that by combining the bent-loop mode with the T-shaped dual-arm mode, the antenna pair achieves favorable operational performance across the dual frequency bands while maintaining high isolation between the respective port regions, thereby successfully validating the proposed self-decoupling mechanism.

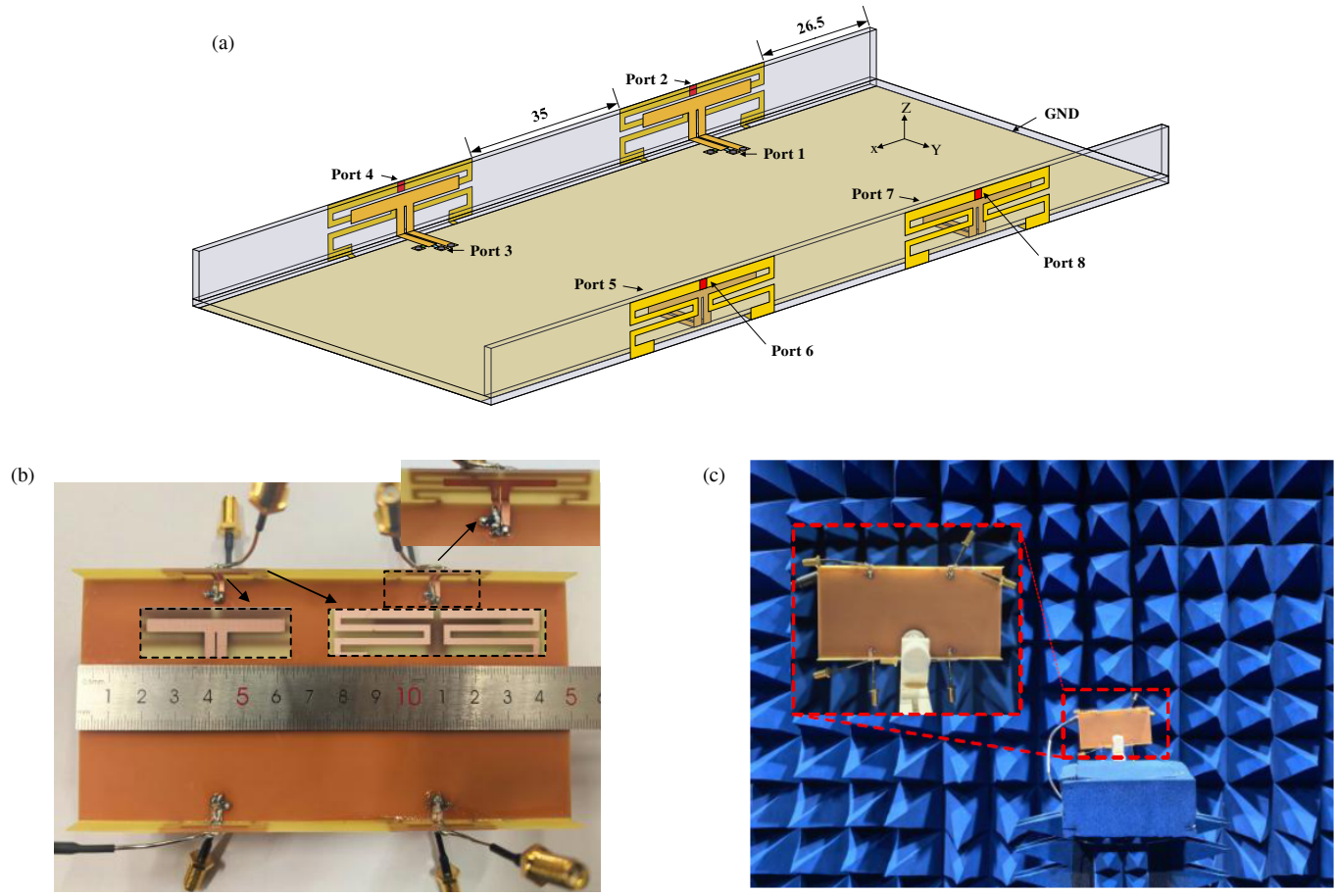

FIGURE 8. Eight-antenna MIMO array. (a) Geometry of the proposed antenna array, (b) fabricated prototype of the antenna array, and (c) measurement in an anechoic chamber.

3. EIGHT-ANTENNA MIMO ARRAY

3.1. Eight-Antenna MIMO Array Demonstration

As shown in Figure 8(a), four antenna pairs are symmetrically arranged on the inner and outer surfaces of the frame, forming an eight-antenna MIMO array. The spacing between adjacent antennas on the same side is 35 mm, and a 1 mm clearance is maintained between the metal ground plane and the edge of the smartphone frame. The array is fully integrated within the smartphone frame without the incorporation of any additional decoupling structures. Figure 8(b) presents a photograph of the fabricated eight-antenna MIMO array prototype. Figure 8(c) depicts the measurement setup of the antenna array inside an anechoic chamber.

3.2. Simulated and Measured Performance

Figure 9 presents the simulated and measured performance metrics of the eight-antenna MIMO array. Figure 9(a) compares the simulated and measured reflection coefficients. Due to the symmetry of the array configuration, only Port 1 and Port 2 are shown as representative examples. It can be observed that the antenna array covers the 3.4–3.6 GHz and 5.1–5.76 GHz frequency bands. Within these operating bands, the simulated and measured reflection coefficients are in good agreement and remain below -6 dB. Figure 9(b) shows the simulated and measured transmission coefficients. The measured results agree reasonably well with the simulations, although a slight shift in the frequency of the decoupling null is observed. The transmission coefficients stay below -15 dB. Despite the presence of near-field coupling among distinct antenna pairs, favorable isolation between different ports is maintained.

Figure 9(c) gives the simulated and measured total antenna efficiencies. For Port 1, the measured efficiencies exceed 75% and 74% in the lower and upper bands, respectively, while for Port 2, the corresponding efficiencies are better than 72% and 70%. Figure 9(d) displays the simulated and measured ECCs. In the simulation and measurement analysis presented in this work, the measured total efficiency exceeds 70% across the entire operating band, and the port-to-port isolation remains below -15 dB. Under such loss conditions, the difference between the ECC values obtained from the S-parameter method and those from the far-field integration method is negligible, which is sufficient for accurately evaluating the diversity performance. Therefore, all ECC values are approximately computed based on the S-parameters. For the i-th and j-th antenna elements, the ECC is calculated using the following formula:

$$\rho_{e,ij} = \frac{\left|S_{ii}^{*}S_{ij} + S_{ji}^{*}S_{jj}\right|^{2}}{\left(1-\left(|S_{ii}|^{2}+|S_{ji}|^{2}\right)\right)\left(1-\left(|S_{jj}|^{2}+|S_{ij}|^{2}\right)\right)} \quad (4)$$

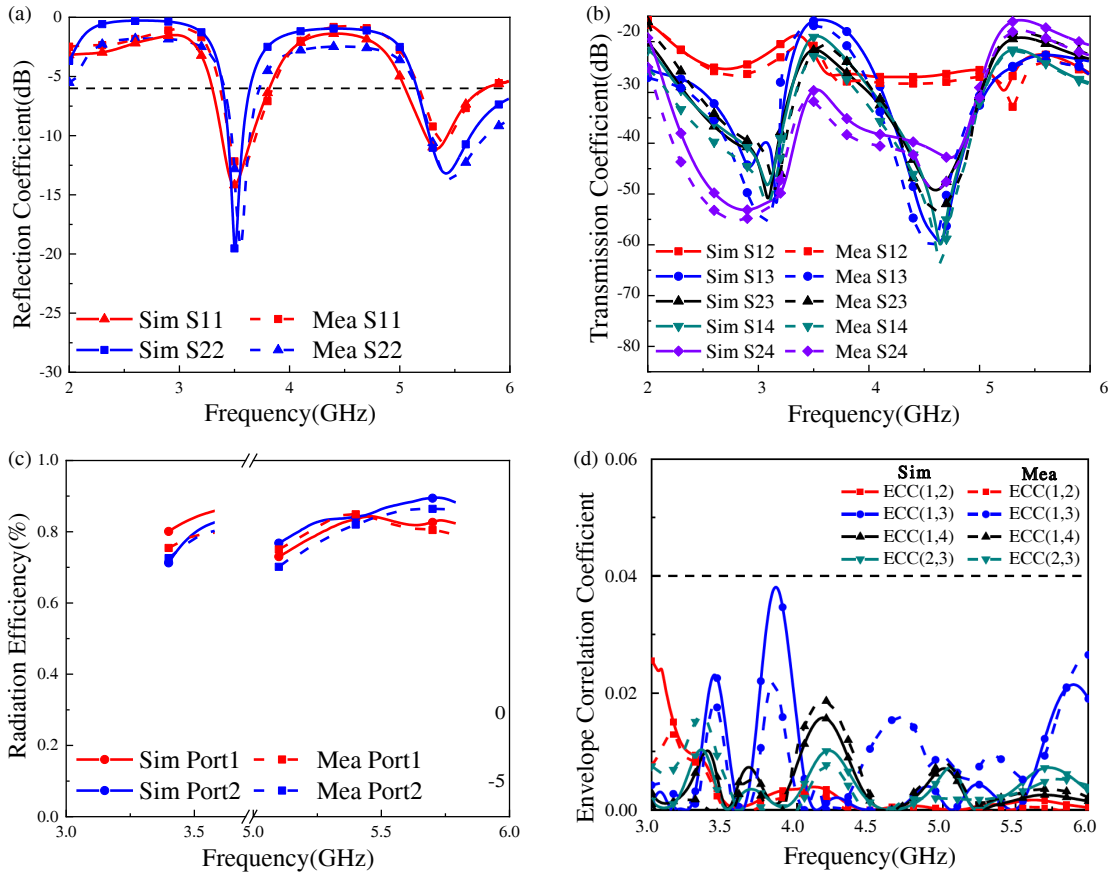

FIGURE 9. Simulation and measured results. (a) Reflection coefficients, (b) transmission coefficients, (c) total efficiencies of the 8 × 8 MIMO system, and (d) envelope correlation coefficients.

TABLE 1. Comparison with other reported antennas.

Ref.	Port	Decoupling method	Operating Frequency (GHz)	Isolation of Antenna Pair (dB)	Radiation efficiency (%)	ECC
[11]	8	Modal cancellation	3.3–4.2	> 10.5	> 63.1	-
[12]	12	Modal cancellation	3.4–3.6	> 11	> 51	< 0.14
[13]	8	Mode orthogonality	3–3.5	> 12	> 58.9	< 0.11
[14]	8	Mode orthogonality	3.4–3.6	> 24	> 61	-
[19]	8	Mode orthogonality	4.4–5	> 26.4	> 56.8	-
[20]	8	Mode orthogonality	3.4–3.6, 4.4–5	> 12.8	> 68	< 0.18
[21]	2	Modal cancellation	3.4–3.6, 4.8–5	> 20	> 71	-
Proposed	8	Mode orthogonality	3.4–3.6, 5.1–5.76	> 15	> 70	< 0.04

where S_{ii} and S_{jj} are the reflection coefficients at the i-th and j-th ports; S_{ij} and S_{ji} are the transmission coefficients between ports i and j; and * denotes the complex conjugate. Across the entire operating frequency range, both simulated and measured ECC values remain below 0.04, indicating satisfactory spatial diversity performance.

Figure 10 depicts the simulated and measured two-dimensional (2D) radiation patterns in the E-plane and H-plane at the resonant frequencies of 3.5 GHz and 5.48 GHz. The simulated and measured pattern traces exhibit consistent trends, further corroborating the feasibility of the self-decoupling mechanism inherent to the proposed structure.

4. PERFORMANCE COMPARISON

Table 1 presents a comparison between the proposed antenna and designs reported in the existing literature. As can be observed, the majority of prior works [11–14, 19], despite employing self-decoupling schemes, are limited to single narrow frequency band operation. The dual-band self-decoupling antenna system proposed in [20] employs a 2-mm-thick side frame, whose thickness limits its application in 5G terminal devices. Compared with the design in [20], the proposed antenna achieves slightly improved isolation and radiation efficiency; . Compared with the dual-band antenna pair design in [21], the

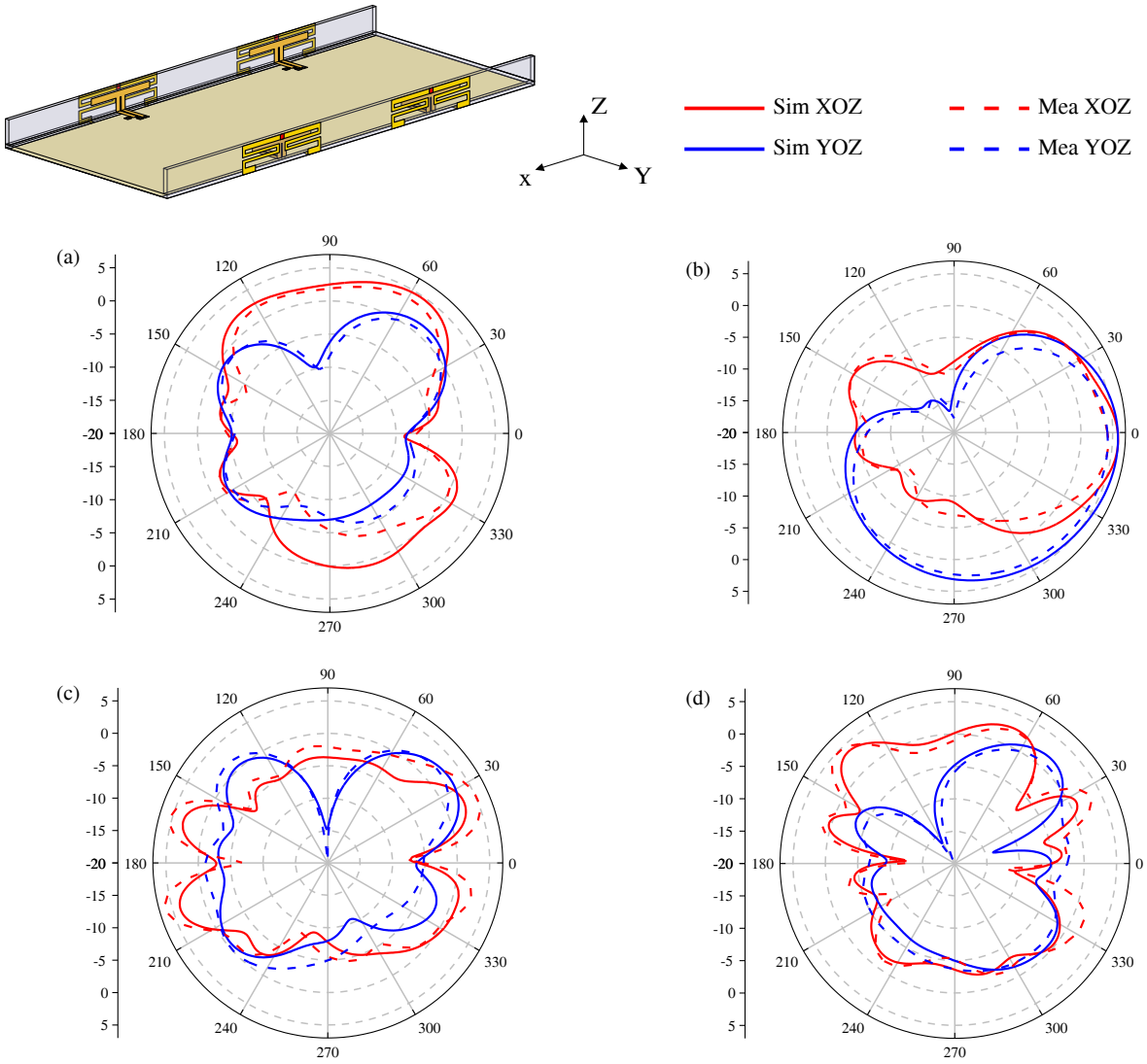

FIGURE 10. Simulated and measured radiation patterns in both XOZ and YOZ. (a) Port 1 is excited at 3.5 GHz, (b) port 2 is excited at 3.5 GHz, (c) port 1 is excited at 5.48 GHz, and (d) port 2 is excited at 5.48 GHz.

proposed design exhibits a wider fractional bandwidth in the high band. The antenna presented in this work features a compact structure and a high level of integration, realizing dual-band operation and high isolation within a constrained volume, thereby providing an effective technical reference for future 5G smartphone antenna designs.

5. CONCLUSION

This paper has presented a highly integrated, high-isolation dual-band antenna pair suitable for integration with although its high-band relative bandwidth is slightly narrower, dual-band operation is still successfully attained in the frame of a 5G smartphone. Based on the principle of mode orthogonality, the design skillfully incorporates a T-shaped dual-arm antenna and a bent-loop antenna within the confined space of the smartphone frame, thereby exciting multiple in-phase and anti-phase modes across two frequency bands. Under a closely spaced arrangement and without the need for additional decoupling structures, the antenna pair exhibits superior isolation exceeding 20 dB. Experimental results demonstrate that a MIMO antenna array, formed by symmetrically arranging four such antenna pairs, effectively covers the 3.4–3.6 GHz and 5.1–5.76 GHz frequency bands. The ECC between any two ports remains below 0.04, and the measured total efficiencies in the two bands exceed 70% and 72%, respectively. This design successfully unifies multi-band operation and self-decoupling characteristics within the smartphone frame, offering an effective technical reference for future multi-antenna integration in 5G mobile terminals.

ACKNOWLEDGEMENT

This work was supported in part by the Natural Science Research Project of Anhui Educational Committee under Grant no. 2025AHGXZK31006, in part by the Research Foundation of Jiangsu Engineering Research Center for Bionics Control Technology and Equipment under No. FSKZ202503, in part by the Anhui International Joint Research Center for Ancient Architecture Intellisensing and Multi-Dimensional Modeling un-

der No. GJZZX2025KF03, in part by the Graduate Innovation Fund of Anhui University of Science and Technology under grant No.2026cx2056.

REFERENCES

[1] Ren, W., Z. Wang, W. Nie, W. Mu, C. Li, M. Wang, and W. You, "A 12-unit asymmetric mirror-coupled loop antenna for 5G smartphones," *Progress In Electromagnetics Research C*, Vol. 145, 141–152, 2024.

[2] Wang, Z., S. Liu, W. Nie, M. Yang, and C. Li, "Broadband eight-element MIMO antenna with high isolation for 5G smartphone applications," *Progress In Electromagnetics Research C*, Vol. 152, 209–219, 2025.

[3] Wang, L., H. Lin, and C. Li, "Miniaturized wideband filtering antenna without additional filtering structures," *Progress In Electromagnetics Research C*, Vol. 163, 222–230, 2026.

[4] Zeng, W.-F., F.-C. Chen, and Q.-X. Chu, "Bandwidth-enhanced 5G mobile phone antenna pair with tunable electric field null," *IEEE Transactions on Antennas and Propagation*, Vol. 71, No. 2, 1960–1964, 2023.

[5] Hei, Y. Q., J. G. He, and W. T. Li, "Wideband decoupled 8-element MIMO antenna for 5G mobile terminal applications," *IEEE Antennas and Wireless Propagation Letters*, Vol. 20, No. 8, 1448–1452, 2021.

[6] Cui, L., J. Guo, Y. Liu, and C.-Y.-D. Sim, "An 8-element dual-band MIMO antenna with decoupling stub for 5G smartphone applications," *IEEE Antennas and Wireless Propagation Letters*, Vol. 18, No. 10, 2095–2099, 2019.

[7] Megahed, A. A., M. Abdelazim, E. H. Abdelhay, and H. Y. M. Soliman, "Sub-6 GHz highly isolated wideband MIMO antenna arrays," *IEEE Access*, Vol. 10, 19 875–19 889, 2022.

[8] Ren, A., H. Yu, L. Yang, Z. Huang, Y. Liu, and J. Hou, "Massive 16-element wideband decoupled pairs with high integration for 5G smartphones," *IEEE Antennas and Wireless Propagation Letters*, Vol. 23, No. 12, 4114–4118, 2024.

[9] Chang, L., G. Zhang, and H. Wang, "Dual-band antenna pair with lumped filters for 5G MIMO terminals," *IEEE Transactions on Antennas and Propagation*, Vol. 69, No. 9, 5413–5423, 2021.

[10] Tian, X. and Z. Du, "Dual-feed shared-radiator metal-frame full-screen mobile phone antenna for GPS and LTE bands with a dual-function capacitor," *IEEE Transactions on Antennas and Propagation*, Vol. 71, No. 10, 8314–8319, 2023.

[11] Sun, L., Y. Li, Z. Zhang, and H. Wang, "Self-decoupled MIMO antenna pair with shared radiator for 5G smartphones," *IEEE Transactions on Antennas and Propagation*, Vol. 68, No. 5, 3423–3432, 2020.

[12] Yang, B., Y. Xu, J. Tong, Y. Zhang, Y. Feng, and Y. Hu, "Tri-port antenna with shared radiator and self-decoupling characteristic for 5G smartphone application," *IEEE Transactions on Antennas and Propagation*, Vol. 70, No. 6, 4836–4841, 2022.

[13] Sun, L., Y. Li, Z. Zhang, and Z. Feng, "Wideband 5G MIMO antenna with integrated orthogonal-mode dual-antenna pairs for metal-rimmed smartphones," *IEEE Transactions on Antennas and Propagation*, Vol. 68, No. 4, 2494–2503, 2020.

[14] Xu, H., S. S. Gao, H. Zhou, H. Wang, and Y. Cheng, "A highly integrated MIMO antenna unit: Differential/common mode design," *IEEE Transactions on Antennas and Propagation*, Vol. 67, No. 11, 6724–6734, 2019.

[15] Ren, A., H. Yu, L. Yang, Z. Huang, Z. Zhang, and Y. Liu, "A broadband MIMO antenna based on multimodes for 5G smartphone applications," *IEEE Antennas and Wireless Propagation Letters*, Vol. 22, No. 7, 1642–1646, 2023.

[16] Deng, C., X. Cao, D. Li, and W. Yu, "Compact dual-band MIMO antenna with shared decoupling structure for 5G mobile terminals," *IEEE Antennas and Wireless Propagation Letters*, Vol. 22, No. 6, 1281–1285, 2023.

[17] Ren, Z., A. Zhao, and S. Wu, "MIMO antenna with compact decoupled antenna pairs for 5G mobile terminals," *IEEE Antennas and Wireless Propagation Letters*, Vol. 18, No. 7, 1367–1371, 2019.

[18] Chang, L., Y. Yu, K. Wei, and H. Wang, "Orthogonally polarized dual antenna pair with high isolation and balanced high performance for 5G MIMO smartphone," *IEEE Transactions on Antennas and Propagation*, Vol. 68, No. 5, 3487–3495, 2020.

[19] Sui, J., C. Huang, J. Li, X. Zhu, and D. Li, "Wideband aperture-overlapped MIMO antennas naturally integrating mode orthogonal and parasitic decoupling schemes," *IEEE Antennas and Wireless Propagation Letters*, Vol. 23, No. 8, 2441–2445, 2024.

[20] Hu, W., Q. Li, H. Wu, Z. Chen, L. Wen, W. Jiang, and S. Gao, "Dual-band antenna pair with high isolation using multiple orthogonal modes for 5G smartphones," *IEEE Transactions on Antennas and Propagation*, Vol. 71, No. 2, 1949–1954, 2023.

[21] Tang, W., J. Sui, Y. Wang, D. Li, J. Li, and X. Zhu, "Dual-band and wideband self-decoupled MIMO antennas with four hybrid modes," *IEEE Antennas and Wireless Propagation Letters*, Vol. 23, No. 10, 3272–3276, 2024.